Available online at www.sciencedirect.com

SCIENCE DIRECT

CARBON

Carbon 44 (2006) 1503–1510

www.elsevier.com/locate/carbon

Control of catalyst particle crystallographic orientation in vertically aligned carbon nanofiber synthesis

J.D. Fowlkes [a,b,*], A.V. Melechko [a,b], K.L. Klein [a,b], P.D. Rack [b], D.A. Smith [b], D.K. Hensley [a,c,d], M.J. Doktycz [d,e], M.L. Simpson [a,b,c,d]

[a] *Molecular-Scale Engineering and Nanoscale Technologies Research Group, Oak Ridge National Laboratory, P.O. Box 2008, MS 6006, Oak Ridge, TN 37831-6006, United States*

[b] *Materials Science and Engineering Department, The University of Tennessee, Knoxville, TN 37996-2200, United States*

[c] *Condensed Matter Sciences Division, Nanobiological Materials Sciences, Oak Ridge National Laboratory, P.O. Box 2008, MS 6033, Oak Ridge, TN 37831-6033, United States*

[d] *Center for Nanophase Materials Sciences, Oak Ridge National Laboratory, Oak Ridge, TN 37831-6056, United States*

[e] *Life Sciences Division, Oak Ridge National Laboratory, P.O. Box 2008, MS 6123, Oak Ridge, TN 37831-6123, United States*

Received 23 March 2005; accepted 6 December 2005
Available online 24 January 2006

Abstract

Vertically aligned carbon nanofibers (VACNF) have been synthesized where the crystallographic orientation of the initial catalyst film was preserved in the nanoparticle that remained at the nanofiber tip after growth. A substantial percentage of catalyst particles (75%), amounting to approximately 200 million nanofibers over a 100 mm Si wafer substrate, exhibited a sixfold symmetry attributed to a cubic Ni(1 1 1)||Si(0 0 1) orientation relationship which was verified by X-ray diffraction studies. The Ni catalyst films were prepared by rf-magnetron sputtering under substrate bias conditions to yield a single (1 1 1) film texture. The total energy of the Ni thin film was estimated by calculating the sum of the surface free energy and strain energy. The total film energy was minimized by the evolution of the plane of lowest surface free energy, the (1 1 1) texture. This result was in agreement with X-ray diffraction measurements. The preferred orientation present in the Ni catalyst film prior to nanofiber growth was preserved in the Ni catalyst particles throughout the VACNF growth process. The Ni catalyst particles at the nanofiber tips were not pure single crystals but rather consisted of a mosaic structure of Ni nanocrystallites embedded within Ni catalyst nanoparticles (200–400 nm). The tip-located nanoparticles exhibited a faceted, crystal morphology with the faceting transferred to the underlying carbon nanofiber during the growth process. The possibility of precisely and accurately controlling VACNF growth velocity over macroscopic wafer dimensions with uniformly aligned catalyst particles is discussed.
© 2006 Elsevier Ltd. All rights reserved.

Keywords: Carbon fibers; Catalyst; Plasma sputtering; X-ray diffraction; Phase transitions

1. Introduction

Vertically aligned carbon nanofibers have been used to address numerous scientific and technological applications including, electron field emission sources [1–5], atomic force microscopy tips [6,7], gene delivery arrays [8,9], electrochemical probes [10–12], and others [13–15]. Many of the applications require the precise and accurate replication of shape, structure, and morphology of these structures on the nanoscale over macroscopic dimensions, e.g. standard 100 mm diameter Si wafer substrates. The future development of more complex devices based on carbon nanofiber technology requires significant, parallel advances in the controlled synthesis of VACNFs.

VACNFs are grown using the direct-current, plasma enhanced chemical vapor deposition (DC-PECVD) process from ammonia and acetylene gas precursors at

* Corresponding author. Address: Materials Science and Engineering Department, The University of Tennessee, Knoxville, TN 37996-2200, United States. Fax: +1 865 974 4115.
E-mail address: fowlkesjd@ornl.gov (J.D. Fowlkes).

0008-6223/$ - see front matter © 2006 Elsevier Ltd. All rights reserved.
doi:10.1016/j.carbon.2005.12.010

pre-patterned Ni catalyst sites on a Si wafer substrate [16]. Our previous work has demonstrated the role of catalyst composition [17], electrical field [18], and plasma gas composition [19] to the control of VACNF synthesis. Following in this vein, the target of this work is the development of an additional mode of VACNF synthesis control by the manipulation of individual catalyst particle crystallographic orientation. Control of this specific synthesis variable is expected to provide a more uniform, collective nanofiber growth velocity, and generate defined structure for chemical processes reliant upon a unique crystal face for chemical functionality.

In the "tip" type VACNF growth used here, carbon atoms diffuse to the base of the catalyst particles forming a solid fiber consisting of stacked and tapered graphene sheets in which a herringbone type internal atomic configuration is established that lifts the particle off the substrate surface [20]. Further details of the fiber growth process have been described in extensive detail previously [16–21] and will not be revisited here. Catalyst dot patterning by standard lithographic techniques also made discrete particle size control highly feasible. For example, to produce a catalyst particle film from a continuous, nanothick film requires a pre-etch process conducted under DC-PECVD conditions in an ammonia atmosphere which effectively "breaks-up" the continuous film. Solid state diffusion ensues rearranging the film by a bulk, mass transport phenomenon; a process driven by a high substrate temperature $\sim$600–750 °C and the dual effects of ammonia by etching the film and providing energy to catalyst atoms by impinging ions derived from the ammonia gas. The use of a pre-defined catalyst surface matrix avoids complications associated with the pre-etch such as an inconsistent particle size due to the chaotic nature of the plasma etching process and the migration of small catalyst particles on the substrate surface from thermally driven Brownian motion. The film deposition technique of substrate bias, rf-magnetron sputtering was used to deposit both catalyst dot and continuous Ni films.

Ni films have been deposited previously by electron beam evaporation [22–25] as well as by DC plasma sputtering [26] where ion-assisted film bombardment was used during the deposition process. A (200) orientation developed in relatively thick (0.5–1.5 μm) Ni films deposited at increased ion-to-atom flux ratios (0.1) [22]. Kuratani et al. found a predominant (111) preferred orientation and a compressive internal stress in Ni films deposited on Si(001) wafers by evaporation under an ion bombardment of 500 V impinging during film deposition [23]. In addition, they determined that internal film stress is most sensitive to ion bombardment with an energy <2 keV; above 5 keV film stress was relatively insensitive to ion energy [23]. Shi et al. have identified a substrate temperature deposition node at the Movchan–Demchishin T_1–T_2 zone boundary for Ni film deposited on silica where the orientation is split equally among the (111) and (200); at all other deposition temperatures the (111) fiber texture dominates [24]. Popovic et al. induced an orientation change from (111) to (200) at a substrate bias potential of 4.5 keV and an impinging ion-to-atom ratio of 0.040 during electron beam triode ion plating of Ni [25]. In our case, Ni thin films 44–200 nm thick were deposited by rf-magnetron sputtering under rf-substrate bias in order to effect film crystallographic orientation.

An rf power was applied to the Si substrate platform during the magnetron sputtering of Ni thin films in an effort to induce a preferred crystallographic orientation in the internal film structure. A negative DC self-bias develops at the substrate plane that induces Ar ions, generated in the sputtering plasma, to bombard the substrate surface during deposition providing an additional source of energy to adsorbed Ni species. Impacting ions induce atomic rearrangement thereby annihilating substitutional atom vacancies increasing film density. Intrinsic film stresses also develop due the rearrangement and annihilation of these vacancies. Moreover, the Ar ions themselves may incorporate into the film as defects.

2. Experimental

2.1. Ni catalyst film preparation

Ni catalyst films were prepared by radio-frequency magnetron sputtering on patterned and unpatterned (001) 4″ Si wafers. In the case of patterned wafers, 500 nm diameter Ni dots with a 5 μm pitch were prepared by standard, optical projection lithographic techniques. In all cases films were deposited at 298 K under a sputtering pressure of 3 mTorr in 25 $cm^3\ min^{-1}$ Ar. In certain instances a substrate bias (U_B) was applied during the deposition time over a variable range of $-100\ V \geqslant U_B \geqslant 0\ V$. An rf power of 200 W was applied to a nickel foil target and induced a DC self-bias at the target surface of 460 V. The Ni foil (Alfa-Aesar, Puratronic® grade) was 0.5 mm thick and had a purity of 99.994%. The average substrate-to-target distance during sputtering was $\sim$13 cm (an average value is reported here because the sample was rotated during sputtering). A film growth rate of 4.7 nm min^{-1} was determined for these sputtering conditions and all films were deposited $h =$ 100 nm ± 5 nm thick or 150 nm ± 7.5 nm thick. To measure the internal crystal size of the film grains as a function of film thickness, a Ni film with a variable thickness ranging from 44 nm to 200 nm was deposited over a 100 mm Si wafer substrate, under the same conditions listed above.

2.2. VACNF growth

2.2.1. Continuous Ni catalyst films

To create the catalyst nanodots for VACNF growth, the continuous Ni catalyst films were pre-etched in an ammonia plasma ($Q_{NH_3} = 80\ cm^3\ min^{-1}$, $P_T = 8$ Torr) for 1 min under a DC bias of 440 V ($i = 400$ mA) in the DC-PECVD growth chamber, where Q is the gas flow rate at standard temperature and pressure. The substrate temperature was

set to 750 °C during the pre-etch. Subsequently, acetylene (C_2H_2) was added to the chamber atmosphere at $Q_{C_2H_2} = 30\ cm^3\ min^{-1}$ and the total gas pressure was increased to 10 Torr under the DC plasma conditions. The substrate temperature remained set at 750 °C during the growth cycle which lasted 10 min.

2.2.2. VACNF growth from Ni catalyst dots

A pre-etch cycle was not required for the dot Ni catalyst films. VACNF growth proceeded at 3 Torr ($Q_{NH_3} = 80\ cm^3\ min^{-1}$, $Q_{C_2H_2} = 45\ cm^3\ min^{-1}$) with a lower substrate temperature of 700 °C and a DC bias of 528 V ($i = 350$ nA) for 10 min.

3. Results and discussion

Fig. 1 shows the XRD results from a θ–2θ scan, using the parafocusing diffractometer geometry, of a continuous Ni film, 100 nm thick supported on a Si(001) wafer substrate. The XRD pattern from a purely polycrystalline Ni foil, is also shown superimposed in Fig. 1. Three major reflections were observed in the XRD pattern for the Ni foil at $2\theta = 44.53$, 51.85, and 76.41 which correspond to the (111), (200), and (220) reflections, respectively. The foil shows the expected peak 2θ positions and peak intensity ratios characteristic of a bulk polycrystalline Ni sample as compared against a literature Ref. [27].

The (111) peak reflection was the only peak of substantial magnitude observed in the XRD scan of the sputtered film; the (200) and (220) peak reflections, observed in the Ni target foil, were not observed in the XRD data for the sputtered film. The observation of one substrate peak indicates a near epitaxial film exhibiting the characteristic single crystallographic orientation. However, as shown below the estimated crystallite size for this film is significantly less than the film thickness, indicating that film is not truly a single crystal as numerous grain boundaries exist within the film structure. Moreover, amorphous regions likely co-exist with the crystalline grains due to the low temperature of the substrate during film deposition.

A film was also deposited with a substrate bias of 0 V as a reference sample in order to determine the effect of the substrate bias on Ni film quality (Fig. 2). The (200) reflection was observed in the XRD θ–2θ scan for the unbiased sample where it was absent in the biased case. The relative magnitude of the integrated intensity for the (111) reflection for both samples was measured to determine the difference in crystallinity among the samples. The additional energy imparted by ion bombardment to the film deposited under bias conditions induced an 8.6× increase in relative crystallinity. The effective thermal migration distance of adsorbed Ni atoms is increased by the ion-to-atom energy transfer under the bias condition. Adsorbed atoms then migrate to high energy surface sites thereby minimizing the surface free energy by forming the equilibrium, crystalline structure over the more energetic amorphous atomic configuration.

The film deposited with the −100 V substrate bias met our catalyst criteria of one strong preferred orientation normal to the substrate plane, and this film was further characterized more carefully by XRD in preparation for VACNF growth and to elucidate the driving force for evolution of the (111) fiber texture. The films were then used as catalysts for the growth of deterministically controlled VACNF synthesis.

The thin film crystallite size was estimated from the X-ray diffraction data by applying the Scherrer equation to the width of the (111) reflection. The Scherrer equation

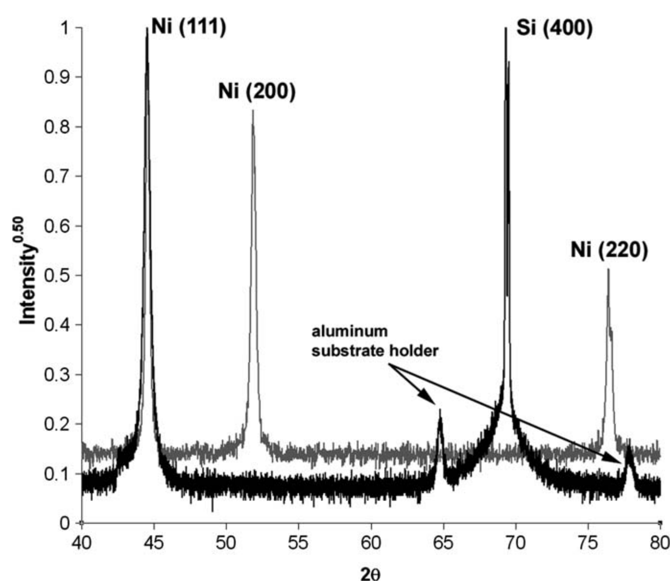

Fig. 1. θ–2θ XRD diffractometer scans from a Ni foil target used during sputtering (light grey) and a textured Ni thin film (bold black), 100 nm thick deposited by rf-magnetron sputtering under a substrate bias of −100 V.

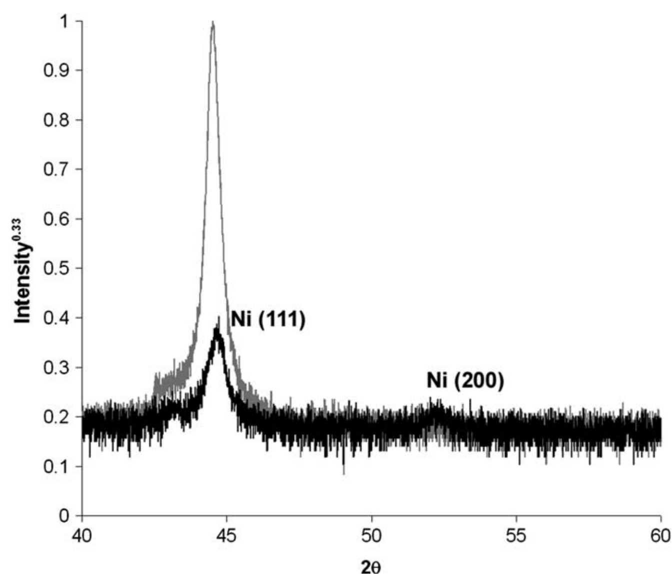

Fig. 2. θ–2θ XRD scans of an unbiased ($U_B = 0$ V, bold black) and biased ($U_B = -100$ V, light grey) thin Ni film ($t = 100$ nm).

for determining crystallite sizes on the order of hundreds of nanometers is

$$d = \frac{0.94\lambda}{B_r \cos\theta} \quad (1)$$

where λ is the X-ray wavelength assumed to be monochromatic, d is the crystallite length dimension in the film thickness direction, B_r is the FWHM of the X-ray reflection after subtracting out instrument broadening effects, and θ is the Bragg angle. An arbitrary X-ray reflection may broaden due to two intrinsic properties of the thin film: (1) lattice strains; and (2) crystallite size induced broadening. However, for 2θ values less than 50° crystallite size effects dominate the peak broadening phenomena [28]. The Ni(1 1 1) reflection fit a Gaussian profile and as a result the following relationship to account for instrument broadening was used

$$B_r^2 = B_o^2 - B_i^2 \quad (2)$$

where B_r is the corrected FWHM, B_o is the FWHM measured from the collected X-ray data, and B_i is the FWHM due to instrument broadening. Table 1 lists the corrected crystallite size results as a function of Ni thin film thickness (h_{Ni}) for a thickness range of 44 nm–200 nm.

The absolute accuracy of the Scherrer equation is questionable for a thin film thickness value of less than ~100 nm. So while the values listed in Table 1 are qualitative, they do show a trend towards smaller grain sizes for thinner films. This result was expected due to the preference for vertical grain growth in thin film materials; in general as film thickness increases, growing grains taper, expanding laterally with increasing dimensions as the film grows thicker. Ni catalyst particles located at the tips of the VACNFs were determined to range in size from ~200–400 nm. The XRD results shown in Table 1 indicate that the catalyst nanoparticles contain a smaller, nanosized subgrain internal structure.

Thin film strain may also be evident in an XRD pattern from a 2θ peak position shift. This strain may be either compressive or tensile and arises as a result of individual atomic vacancies (atomic voids) [29], the microscopic coalescence of voids (microscopic voids) [30], implanted inert gas molecules during the sputtering process [31], and thermal strain possibly arising from a difference in the linear coefficient of thermal expansion between the thin film and substrate. Biaxial, in-plane stresses develop in thin film/substrate architectures when exposed to various strain-inducing environments. Moreover, for thin films containing a preferred crystallographic orientation requires the stress analysis to include the anisotropic, elastic mechanical material response property for correct strain calculations. In general, XRD 2θ peak shifts to lower values indicate a positive strain (lattice expansion) normal to the film/substrate surface and compressive, in-plane stresses. A compressive strain exists normal to the film/substrate surface with tensile, in-plane stresses when a shift to higher 2θ values is observed.

Table 1
A thin, nanocrystalline Ni film was prepared with a film thickness gradient ranging from 44 to 200 nm

Film thickness [nm]	2θ [degrees]	Intensity [$\Delta 2\theta \times$ counts]	d [nm]
200	44.495	2899	29
100	44.488	2017	27
77	44.489	1215	24
56	44.483	752	22
44	44.490	324	18

The film thickness imposed a constraint on the crystallite size in the film; thinner films produced smaller average nanocrystallite sizes. Column 1 lists the thickness of the thin film at the position where the θ–2θ XRD scan was obtained. Column 2 lists the 2θ position of the Ni(1 1 1) reflection while column 3 lists the integrated intensity of the reflection. The last column displays the estimated grain diameter within the thin film.

The total energy of the film was estimated assuming that the internal stress and surface energy were the significant contributing factors to the film energy. The total energy is a function of crystallographic orientation; the texture with the minimum total energy will be the preferred texture that develops parallel to the film surface plane. The estimation was made from XRD data collected on a 100 nm thick Ni film that exhibited a predominant (1 1 1) texture. The internal stress was calculated based on the observed 2θ peak shift of the (1 1 1) reflection. A biaxial compressive stress of $\sigma_1 = \sigma_2 = -90$ MPa was calculated for the film. The surface energy for the two detectable X-ray reflections from the Ni film were estimated from Eq. (9) (supplementary material) to be $\gamma_{111} = 2.23$ eV and $\gamma_{200} = 3.87$ eV. The details of these calculations are provided in the supplementary material section of this paper.

The crystallographic plane with the lowest magnitude of total energy (Eq. (8), Appendix A) will be the preferred texture that develops in the thin film. The total energy of the (1 1 1) and (2 0 0) reflections as a function of film strain and surface energy, assuming a constant film thickness of 100 nm, is shown in Fig. 3.

The computed results for total film energy presented in Fig. 3 indicate that the (1 1 1) texture is the preferred film orientation which is in agreement with the stress estimation calculated from the experimental XRD results (Fig. 1). A compressive stress of −90 MPa was estimated from the 2θ shift in the (1 1 1) reflection. Fig. 3 shows that the Ni thin film has a lower total energy by $\Delta E = \gamma_{111} - \gamma_{200} = -1.64\ \mathrm{J\,m^{-2}}$ with the (1 1 1) surface configuration; at this stress the total energy minimization is dominated by the surface energy term.

Ni(1 1 1) thin films were used as catalyst platforms for the growth of vertically aligned, carbon nanofibers. Continuous, nanoscale Ni thin films as well as Ni dot lithographically patterned thin films, both supported on Si wafer substrates, were prepared to support VACNF growth. Fig. 4 exhibits the characteristic morphology observed for VACNF's grown from (1 1 1) textured, Ni catalyst film. Six-edged Ni particle terminated VACNF's were observed in ~75% of the fibers grown on the textured Ni

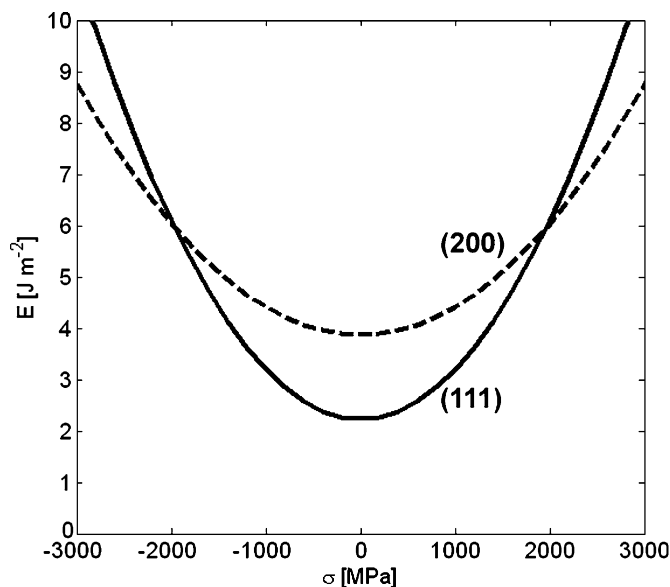

Fig. 3. The total film energy (strain + surface) of the (1 1 1) and (2 0 0) crystallographic faces for a 100 nm thick Ni film. The (1 1 1) texture is preferred for a biaxial stress $\sigma < 2$ GPa above which the (2 0 0) face is the stable surface texture.

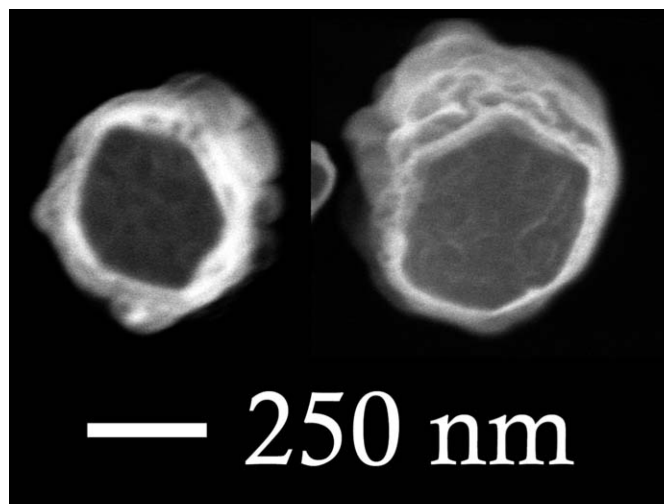

Fig. 4. HRSEM images of two VACNF tips terminated by Ni catalyst tips. The VACNF's were grown from Ni patterned catalyst dots, 100 nm thick and 500 nm in diameter, supported on a 100 mm diameter Si(0 0 1) single crystal wafer. Roughly 75% of the fibers grown on this substrate exhibited Ni terminated VACNF tips with six crystallographic edges per view suggesting a common orientation of Ni catalyst from fiber-to-fiber across the entire wafer surface.

thin film (XRD pattern, bold black, Fig. 1). The particles shown in Fig. 4 were located at the fiber tip as determined by viewing the fibers in the SEM orthogonal to the fiber axis. Further HRSEM analysis revealed that the Ni particles were faceted crystals buried under a thin (~20 nm) sheath of carbon. The faceting of the Ni nanoparticle was transferred into the underlying CNF structure as the carbon fiber itself exhibited a similar faceting phenomena, although in some instances redeposition on the fiber sidewalls covered partially the faceting of the fiber itself. A control catalyst thin film was grown on a Ni thin film that was deposited with no substrate bias. Only 30% of six-edged particles were observed in this film (XRD pattern, bold black, Fig. 2). Moreover, this sample exhibited no specific preference in particle orientation with the catalyst particles exhibiting very little detectable symmetry visually by SEM analysis.

XRD measurements were made on (1 1 1) textured continuous Ni catalyst films prior to VACNF growth (Fig. 5a), after the thin film pre-etch in ammonia to spatially segregate the film into individual nanoparticles (Fig. 5b), and after the growth of the VACNF's (Fig. 5c). XRD was possible following growth due to the near uniform "lift" of the continuous, thin film off the Si substrate surface as a raised layer of suspended Ni nanoparticles. It was found that roughly the same percentage of (1 1 1) textured particles was produced whether VACNF growth was performed using a continuous thin film or discrete, patterned particles so long as the sputtering conditions and substrate were the same for both samples. Moreover, a correlation was determined between the degree of texture (XRD) produced in a continuous, Ni catalyst thin film and the SEM analysis; as the degree of texture increased as the number of six-sided, faceted particles observed during SEM analysis also increased. Hence, XRD results from θ–2θ scans of the continuous thin films were extrapolated to represent the texture condition of the catalyst dot patterns. Fig. 6 shows the XRD θ–2θ scans representative of the film at each of the process temporal nodes illustrated in Fig. 5.

Fig. 6 shows a series of superimposed XRD scans centered about the Ni(1 1 1) reflection. The peak position of the strain-free, Ni(1 1 1) reflection obtained from the Ni target foil is superimposed over the figure as the vertical delta function located at $2\theta = 44.5458°$. The peak obtained from the as-deposited film is centered near perfectly with respect to the foil's (1 1 1) reflection indicating that this film is under a relatively low magnitude of strain. This peak is shifted slightly to lower value of 2θ indicating a slight compressive stress is present in the film but is less than −90 MPa based on the peak's exact position and calculations performed above. The lack of a substantial stress is not surprising as thermal stresses will not develop in a film deposited at room temperature, i.e., minimal thermal cycling took place before, during, and after the sputter deposition of the film. The crystallite size for the 150 nm thick film was roughly 50 nm based on calculations using the Scherrer approximation.

Thermal stresses developed in the film pre-etched in NH_3 gas at an elevated temperature of 750 °C. The temperature ramp from room temperature took approximately 10 min to reach the pre-etch and growth temperature. The film was pre-etched in 10 Torr NH_3 using a DC bias of 414 V producing a steady-state current of 400 mA for 1 min. This combination pre-etch/high temperature cycle acts to roughen the film and effectively converts the film

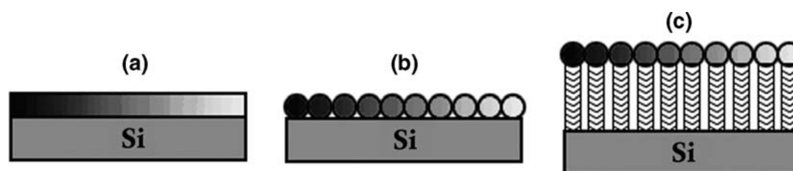

Fig. 5. (a) The continuous 100 nm thick Ni thin film following sputter deposition, (b) the Ni catalyst film is broken up into discrete nanoparticles in response to an NH_3 pre-etch and (c) the raised Ni nanoparticle film after the growth of VACNF's in a gas mixture of C_2H_2–NH_3.

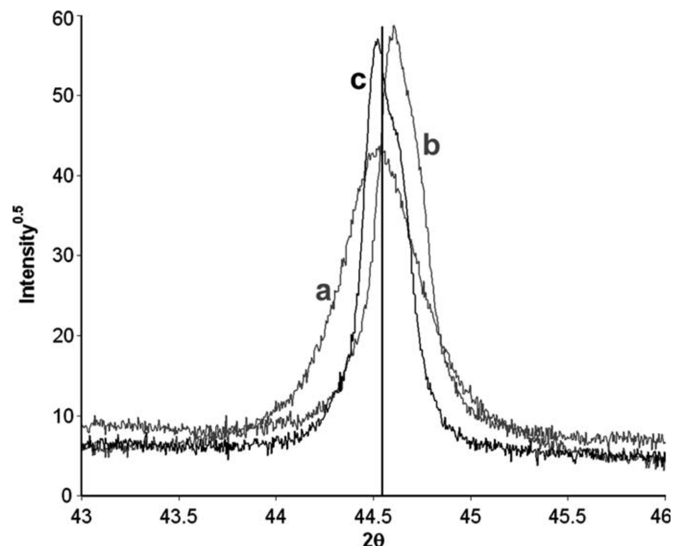

Fig. 6. Ni(1 1 1) reflection following (a) initial thin film deposition at room temperature, (b) the pre-etch to break-up the film into discrete nanoparticles associated with a 2θ peak shift to the right indicating a tensile, biaxial stress that developed in the film due to the thermal cycle, and (c) suspension of the nanoparticle film above the substrate surface by the VACNF's. The film was sputtered using a substrate bias condition of −100 V which produced a strongly (1 1 1) textured film.

into a fine nanoparticle/continuous film conglomerate that inevitably forms discrete, individual nanocrystals during VACNF growth. Scan (b) in Fig. 6 shows the XRD pattern for this sample after the temperature of the substrate had stabilized back to room temperature. The peak shifted to a higher 2θ value of 44.6025° after the pre-etch. This residual stress develops as a result of the difference in thermal expansion coefficients of the thin film and substrate. Recovery, grain growth, and recrystallization phenomenon initiate in the presented order when a metal sample is raised to a $T > 0.3 \times T_m$ ($T \sim 440$ °C, Ni) where T_m is the melting temperature of the bulk metal. These phenomena create a change in the density of the metal as structural vacancy imperfections are annealed out (density increase) or coalesce to form microscopic voids (density decrease). In this specific case, the film was heated to 750 °C. This temperature is adequate to initiate structural imperfection rearrangement by recovery, grain growth and recrystallization. The linear thermal expansion coefficient of Ni ($\alpha_{Ni} = 13.4 \times 10^{-6}\ K^{-1}$) exceeds the value for Si by 3.8×, ($\alpha_{Si} = 3.55 \times 10^{-6}\ K^{-1}$) which places the Ni thin film in compression at high temperature due to the restriction to expansion imposed by the Si substrate. The recovery, grain growth, and recrystallization processes active at the high temperature, lower the film-substrate energy thereby reducing this compressive stress through the thermally activated atomic rearrangement processes. The density of the film increases to reduce the compressive stress. However, once cooled back to room temperature the film experiences a stress reversal to tensile, biaxial stress due to the thermally driven density change. This in-plane, biaxial tensile stress produces a shift to a higher 2θ value as is seen in Fig. 6b and listed in Table 2. Finally, during the VACNF growth step the internal tensile stress is relieved as Ni–Si intimate contact is broken by the nucleation and growth of graphene sheets between the film and substrate (Fig. 6c).

XRD analysis has shown that biased substrates ($U_B = -100$ V) during the subsequent growth of Ni catalyst films develop a (1 1 1) texture. If we assign the [1 1 1] vector to point outward, orthogonal to the Ni catalyst film surface, from the possible members of the <1 1 1> family, e.g., [1 1 1], $[1\bar{1}1]$, $[1\bar{1}\bar{1}]$, …, then the following crystallographic directions lie in the plane of the film (Fig. 7).

The sixfold symmetry observed in the SEM images (Fig. 4) may result from the development of either {0 1 1} or {1 1 2} atomic planes normal to the VACNF growth direction. As shown in Fig. 7, it is impossible to determine which of these possible faces develops from a visual examination of SEM images, if not a mixture of both over many particles, because they would be expected to produce the same particle shape. Further XRD studies are required to elucidate exactly which of these planes, or in what proportion, are exposed.

A proposed growth mechanism of VACNF's gives promise to the idea that a preferred catalyst film orientation would allow for the homogeneous growth of these structures over macroscopic substrate dimensions when exposed to the DC-PECVD VACNF growth process. It has been proposed that the VACNF growth velocity depends fundamentally on the anisotropic growth velocity of graphene sheet based carbon structures. Presumably precise and accurate establishment of one specific crystal

Table 2
Ni(1 1 1) XRD peak parameters as determined from the scans shown in Fig. 6

	Ni film	Ni particles	CNF + Ni
2θ	44.5275	44.6025	44.5225
Intensity	0.967	1.000	0.816
FWHM	0.3408	0.1984	0.1941
d [nm]	50	87	89

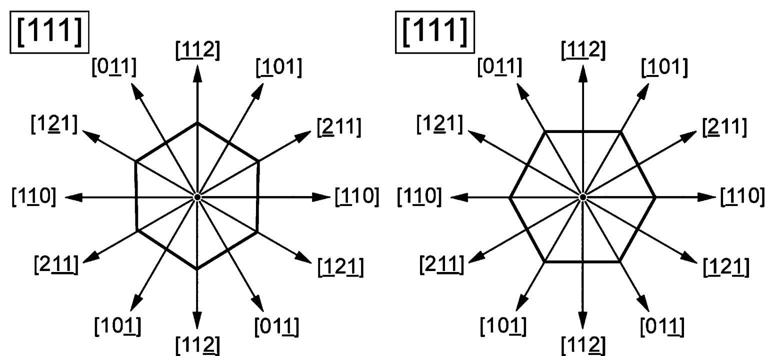

Fig. 7. The various crystallographic directions that lie in the film plane for a Ni film with the (1 1 1) plane parallel to the Si substrate surface; the [1 1 1] direction is directed outward and orthogonal to the film surface.

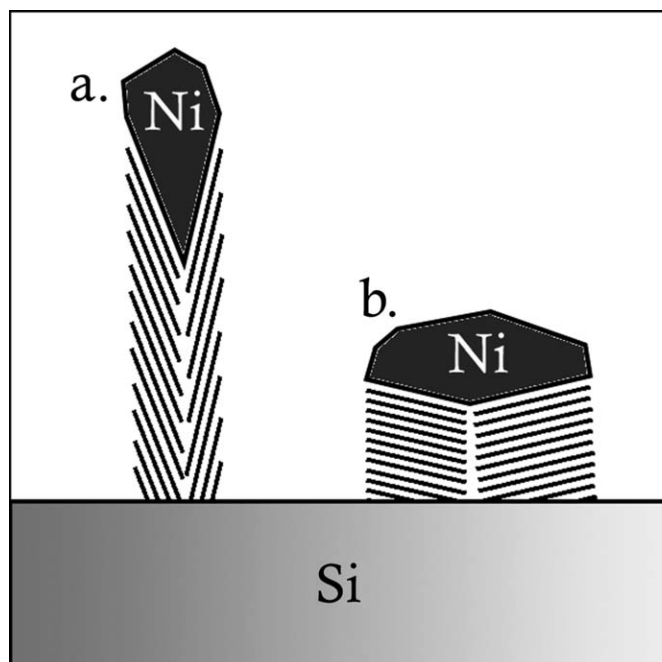

Fig. 8. A schematic illustration of two CNF's that exhibit different growth rates attributed to the difference in the catalyst particle base taper angle; the in-plane graphene sheet growth velocity is conjectured to exceed the out-of-plane graphene sheet nucleation rate.

particle orientation could allow for a common taper angle among all catalyst particles on a substrate yielding a discrete growth velocity among all fibers and ultimately a uniform fiber height over the whole substrate. The internal structure of VACNF's consists of layered stacks of graphene sheets collectively tilted at a variable angle with respect to the substrate plane (Fig. 8). It is well known that the in-plane, atomic growth velocity of graphene sheet is larger in magnitude than the out-of-plane growth rate of additional sheets [11]. It has been experimentally observed that the VACNF's grow on a framework of tapered graphene sheets which are tilted with respect to the vertical growth direction of the fibers but with a variable taper angle from fiber-to-fiber that depends on the bottom taper of the catalyst particle [16]. The schematic shown in Fig. 8 illustrates a typically observed VACNF cross-section revealing the internal arrangement of graphene carbon planes. The figure also shows the surmised relationship between the fiber vertical growth velocity and the catalyst particle base taper angle. In the case of a shallow taper angle (Fig. 8b) the growth velocity relies more upon out-of-plane graphene sheet nucleation and growth with the result that these VACNF's grow slower than fibers with more acute taper angles (Fig. 8a). Hence, it is possible that a uniform growth height over macroscopic dimensions could be achieved if a singular, discrete taper angle was pre-imparted to all catalyst particles. The results that have been presented here provide a positive step toward this goal by inducing a uniform catalyst particle crystallographic orientation for nearly all particles over a 100 mm Si wafer substrate surface. In future experiments film growth conditions favoring the evolution of the (2 0 0) texture will be explored for the purpose of measuring the VACNF growth velocity with respect to the (1 1 1) texture which should prove a crucial experiment in testing the presented hypothesis.

4. Conclusions

Most remarkable is the fact that the preferred orientation and crystallinity of the Ni film is transferred to the Ni catalyst particles through the chaotic, energetic pre-etch and VACNF growth environments. The control of texture through the growth process cycle is a significant step towards the crucial capability to control *more precisely* the *collective shape and morphology* of VACNF fibers over macroscopic distances. This improvement to growth process stability will increase substantially the chip yield from current multi-level lithography processes that rely on high yields to probe the complex variable space of nano-bio merged applications where, VACNF's are the pivotal physical interface between inorganic nano and organic bio materials.

Acknowledgements

This research was supported by NIH Grant EB000657 and the Materials Sciences and Engineering Division

Program of the DOE Office of Science (MLS). This work was performed at The University of Tennessee and the Oak Ridge National Laboratory, managed by UT-Battelle, LLC, for the US DOE under Contract No. DE-AC05-00OR22725. A portion of this research was conducted at the Center for Nanophase Materials Sciences, which is sponsored at Oak Ridge National Laboratory by the Division of Scientific User Facilities, US Department of Energy.

Appendix A. Supplementary data

Supplementary data associated with this article can be found, in the online version, at doi:10.1016/j.carbon.2005.12.010.

References

[1] Gan B, Ahn J, Zhang Q, Yoon SF, Huang QF, Yang H, et al. Branching carbon nanotubes deposited in HFCVD system. Diamond Relat. Mater. 2000;9:897–900.

[2] Guillorn MA, Melechko AV, Merkulov VI, Ellis ED, Britton CL, Simpson ML, et al. Operation of a gated field emitter using an individual carbon nanofiber cathode. Appl Phys Lett 2001;79:3506–8.

[3] Guillorn MA, Melechko AV, Merkulov VI, Ellis ED, Simpson ML, Baylor LR, et al. Microfabricated field emission devices using carbon nanofibers as cathode elements. J Vac Sci Technol B 2001;19:2598–601.

[4] Guillorn MA, Melechko AV, Merkulov VI, Hensley DK, Simpson ML, Lowndes DH. Self-aligned gated field emission devices using single carbon nanofiber cathodes. Appl Phys Lett 2002;81:3660–2.

[5] Guillorn MA, Yang X, Melechko AV, Hensley DK, Hale MD, Merkulov VI, et al. Vertically aligned carbon nanofiber-based field emission electron sources with an integrated focusing electrode. J Vac Sci Technol B 2004;22:35–9.

[6] Cui H, Kalinin SV, Yang X, Lowndes DH. Growth of carbon nanofibers on tipless cantilevers for high resolution topography and magnetic force imaging. Nano Lett 2004;4:2157–61.

[7] Ye Q, Cassell A, Liu H, Chao KJ, Han J, Meyyappan M. Large-scale fabrication of carbon nanotube probe tips for atomic force microscopy critical dimension imaging applications. Nano Lett 2004;4:1301–8.

[8] McKnight TE, Melechko AV, Griffin GD, Guillorn MA, Merkulov VI, Serna F, et al. Intracellular integration of synthetic nanostructures with viable cells for controlled biochemical manipulation. Nanotechnology 2003;14:551–6.

[9] McKnight TE, Melechko AV, Hensley DK, Mann DGJ, Griffin GD, Simpson ML. Tracking gene expression after DNA delivery using spatially indexed nanofiber arrays. Nano Lett 2004;4:1213–9.

[10] McKnight TE, Melechko AV, Guillorn MA, Merkulov VI, Doktycz MJ, Culbertson CT, et al. Effects of microfabrication processing on the electrochemistry of carbon nanofiber electrodes. J Phys Chem B 2003;107:10722–8.

[11] McKnight TE, Melechko AV, Austin DW, Sims T, Guillorn MA, Simpson ML. Microarrays of vertically-aligned carbon nanofiber electrodes in an open fluidic channel. J Phys Chem B 2004;108:7115–25.

[12] Guillorn MA, McKnight TE, Melechko AV, Merkulov VI, Britt PF, Austin DW, et al. Individually addressable vertically aligned carbon nanofiber-based electrochemical probes. J Appl Phys 2002;91:3824–8.

[13] Baylor LR, Lowndes DH, Simpson ML, Thomas CE, Guillorn MA, Merkulov VI, et al. Digital electrostatic electron-beam array lithography. J Vac Sci Technol B 2002;20:2646–50.

[14] Zhang L, Melechko AV, Merkulov VI, Guillorn MA, Simpson ML, Lowndes DH, et al. Controlled transport of latex beads through vertically aligned carbon nanofiber membranes. Appl Phys Lett 2002;81:135–7.

[15] Merkulov VI, Lowndes DH, Wei YY, Eres G, Voelkl E. Patterned growth of individual and multiple vertically aligned carbon nanofibers. Appl Phys Lett 2000;76:3555–7.

[16] Fletcher BL, Hullander ED, Melechko AV, McKnight TE, Klein KL, Hensley DK, et al. Microarrays of Biomimetic Cells Formed by the Controlled Synthesis of Carbon Nanofiber. Nano Lett 2004;4:1809–14.

[17] Klein KL, Melechko AV, Rack PD, Fowlkes JD, Meyer HM, Simpson ML. Cu–Ni composition gradient for the catalytic synthesis of vertically aligned carbon nanofibers. Carbon 2005;43:1857–63.

[18] Merkulov VI, Melechko AV, Guillorn MA, Lowndes DH, Simpson ML. Alignment mechanism of carbon nanofibers produced by plasma-enhanced chemical-vapor deposition. Appl Phys Lett 2001;79:2970–2.

[19] Melechko AV, Merkulov VI, McKnight TE, Guillorn MA, Klein KL, Lowndes DH, et al. Vertically aligned carbon nanofibers and related structures: controlled synthesis and directed assembly. J Appl Phys 2005;97:041301-1-39.

[20] Melechko AV, Merkulov VI, Lowndes DH, Guillorn MA, Simpson ML. Transition between 'base' and 'tip' carbon nanofiber growth modes. Chem Phys Lett 2002;356:527–33.

[21] Merkulov VI, Hensley DK, Melechko AV, Guillorn MA, Lowndes DH, Simpson ML. Control mechanisms for the growth of isolated vertically aligned carbon nanofibers. J Phys Chem B 2002;106:10570–7.

[22] Popovic N, Bogdanov Z, Goncic B, Zec S, Rakocevic Z. The influence of ion bombardment intensity during deposition on nickel films microstructure. Thin Solid Films 1999;344:75–80.

[23] Kuratani N, Murakami Y, Imai O, Ebe A, Nishiyama S, Ogata K. Internal stresses in nickel films prepared by ion beam and vapor deposition. Nucl Instrum Methods Phys Res Sect B—Beam Interact Mater Atoms 1995;106:116–9.

[24] Shi Z, Player MA. Preferred orientations of evaporated Ni films on Mo and SiO_2 substrates. Vacuum 1998;49:257–63.

[25] Popovic N, Dimitrijevic T, Bogdanov Z, Goncic B, Strbac S, Rakocevic Z. Nickel film orientation change by nitrogen ion bombardment during deposition. Vacuum 1997;48:705–8.

[26] Qiu H, Tian Y, Hashimoto M. Evolution of interface diffusion and structure of Ni films sputter-deposited on Si(001). Vacuum 2003;70:493–7.

[27] Swanson HE, Tatge E. Nat Bur Stand (US), Circ 1959;I1:539.

[28] Suryanarayana C, Grant Norton M. X-Ray diffraction: a practical approach. New York: Plenium Press; 1998. p. 215.

[29] Zhigal'ski GP, Jones BK. The physical properties of thin metal films. London & New York: Taylor & Francis; 2003. p. 93.

[30] Muller KH. Stress and microstructure of sputter-deposited thin-films-molecular-dynamics investigations. J Appl Phys 1987;62:1796–9.

[31] Mayrhofer PH, Kunc F, Musil J, Mitterer C. A comparative study on reactive and non-reactive unbalanced magnetron sputter deposition of TiN coatings. Thin Solid Films 2002;415:151–9.